Synthetic aperture superresolved microscopy in digital lensless Fourier holography by time and angular multiplexing of the object information

Luis Granero,[1] Vicente Micó,[2,*] Zeev Zalevsky,[3] and Javier García[2]

[1]AIDO—Technological Institute of Optics, Color and Imaging, Nicolás Copérnico 7, 46980, Paterna, Spain

[2]Departamento de Óptica, University Valencia, Dr. Moliner, 50, 46100 Burjassot, Spain

[3]School of Engineering, Bar-Ilan University, Ramat-Gan 52900, Israel

*Corresponding author: vicente.mico@uv.es

The resolving power of an imaging system in digital lensless Fourier holographic configuration is mainly limited by the numerical aperture of the experimental setup that is defined by both the restricted CCD size and the presence of a beam splitter cube in front of the CCD. We present a method capable of improving the resolution in such a system configuration based on synthetic aperture (SA) generation by using time-multiplexing tilted illumination onto the input object. Moreover, *a priori* knowledge about the imaged object allows customized SA shaping by the addition of elementary apertures only in the directions of interest. Experimental results are provided, showing agreement with theoretical predictions and demonstrating a resolution limit corresponding with a synthetic numerical aperture value of 0.45.   © 2010 Optical Society of America

OCIS codes: 050.1940, 090.1995, 100.2000, 100.6640, 110.0180, 110.1650.

1. Introduction

In 1873, Abbe established that the resolving power in imaging systems is limited by the wave nature of light [1]. Since then, the ability to improve the resolving power of imaging systems beyond the limit imposed by diffraction has become a widely studied topic in applied optics. But the beginning of super-resolution did not start until Françon reported his work in 1952 [2]. It was a time-multiplexing approach based on the synchronized movement of two pinholes, one over the object and another one at the image plane through an optical imaging system. Thus, by spatial scanning the whole object field of view, the approach provides two-dimensional (2D) images via point-by-point imaging of the input object.

After Françon's idea, many other superresolving approaches were reported using information theory as a starting point [3,4]. In summary, since the number of degrees of freedom (channels) of an imaging system remains constant, any degree of freedom in the system could be extended above the classical limit if any other channel is proportionally reduced [5,6]. In that sense, the resolution limit imposed by diffraction could be improved by multiplexing the object's spatial-frequency information in any other channel if the object is independent to such a degree of freedom [7]. Thus, time-multiplexing superresolution encodes the object's spatial-frequency information into the temporal degree of freedom because its amplitude distribution does not vary in time. The encoded object information passes through the limited system's aperture in different time slots, and the remaining problem is how to recover and decode the encoded information.

The classical way to perform such an encoding-decoding process is by using diffraction gratings [5–7]. However, and as Abbe pointed out in his paper [1], another way to increase the resolution of an

imaging system is by tilting the illumination with respect to the optical axis because, then, high order frequency bands are diffracted on axis. So, we can establish an equivalence between the grating's diffraction orders and a set of tilted beams (on-axis and off-axis beams), where each tilted beam produces a given frequency shift in the object's spectrum, depending on its oblique illumination angle. Once again, the point is to recover and reposition each additional high-frequency band to its original location in the object's spectrum, that is, to its original diffracted angle when on-axis illumination is considered. Interferometric image plane recording [8–10] allows the rearrangement of the spatial information corresponding with each transmitted frequency band.

Tilted beam illumination has been applied to superresolution purposes since Ueda and Sato reported the recording of a multiexposed hologram composed of the coherent superposition of a set of images obtained sequentially under different oblique illumination conditions [11]. From then to now, the combination of tilted beam illumination and interferometric recording as a way to get superresolution has been applied to classical holography [11–13], digital holography [14–16], and mainly to digital holographic microscopy [17–23]. Essentially, time-multiplexing superresolution by tilted beams produces a synthetic enlargement in the limited system aperture. This synthetic aperture (SA) is equivalent to a CCD camera with greater size [14–16,24–30] or to a microscope objective with a higher numerical aperture (NA) value [17–23] for applications in digital holography and digital holographic microscopy, respectively.

Recently proposed, digital in-line holographic microscopy combines a Gabor optical implementation and digital reconstruction by numerical processing provided by computers [31–34]. Using this method, experimental results showing an NA value between 0.2 and 0.3 were reported [34]. However, the previous concept is restricted to weak diffraction assumptions as was assumed in the original Gabor concept [35]. In that sense, digital in-line holography considering an external reference beam has been also reported extensively in the literature [36]. But the insertion of a reference beam in the recording plane is usually performed by placing a beam splitter in front of the CCD. Thus, the input object cannot be placed close to the CCD in order to achieve high NA. So, the maximum achievable resolution is limited.

In this paper, we demonstrate superresolution capabilities in microscopy of tilted beam illumination and interferometric recording in a digital lensless Fourier holographic architecture based imaging system. Since the CCD size is restricted to a few millimeters (limited aperture of the imaging system) and the sample must be positioned at a few centimeters from the CCD (due to the beam splitter), the resolving power of the imaging setup becomes restricted. However, high order frequency bands can be recovered by using oblique illumination and off-axis holographic recording

in a time sequence. The key is to perform time multiplexing by means of a set of tilted beams having different inclinations. Because of each tilted beam, a different bandpass of the object's spectrum is diffracted on axis and recovered by a filtering process performed over the Fourier transform (FT) of the recorded hologram. Finally, each recovered bandpass image is used to generate an SA expanding the cutoff frequency of the imaging system, or in other words, improving its resolution. Moreover, if it is *a priori* known that the object's spectrum does not contain useful information at specific directions, the time multiplexing illumination stage can be optimized by avoiding those tilted beams corresponding with those useless directions. This fact allows the generation of a customized SA shape in accordance with the *a priori* object information. In this work, experimental demonstration of medium-high NA values ($0.4 <$ SNA < 0.5), covering without gaps the Fourier domain, showing capabilities of customized SA, working without lenses and outside the weak diffraction assumptions imposed by the Gabor regime is reported.

The paper is organized as follows: Section 2 presents both a qualitative description and the mathematical background of the experiment. Section 3 experimentally validates the proposed approach, providing different shapes of synthetic apertures for two different kind of objects (resolution test target and human red blood cells), and Section 4 concludes the paper.

2. Experimental Configuration

A. Qualitative System Description

The proposed experimental setup is depicted in Fig. 1. It is based on a Mach–Zehnder interferometric configuration in which an He–Ne laser beam is split in two branches. In the first one (imaging branch), the object under test is illuminated in transmission mode and a Fresnel diffracted pattern is recorded by a CCD imaging device. Such a diffracted pattern is combined at the CCD plane with a second beam incoming from the reference branch by using a beam splitter cube. The reference beam is an off-axis spherical divergent wavefront having the particularity that the distance "d" between the object and the CCD [see Fig. 1] is equal to the distance between the point source [focal plane of the FT lens in Fig. 1] and the CCD. This configuration defines a digital lensless Fourier transforming holographic setup where whole information about the complex diffracted wavefront at the input object can be recovered at the Fourier domain of the recorded hologram, since off-axis recording avoids the overlapping between the different holographic diffraction orders.

Using this experimental assembly, the FT of the recorded hologram performs the recovery of the focused bandpass image of the object under test. When on-axis illumination is used [Fig. 1(a)], the focused image at the Fourier domain becomes the conventional image provided by the proposed imaging system

architecture. That image will be limited in resolution due to the low NA that is defined by the imaging system and resulting from both the reduced CCD size and the distance between the input object and the CCD.

One way to improve this low NA value is by using a diffraction grating in the imaging arm of the interferometric configuration [27–29]. The grating allows that additional spatial-frequency bands of the spectrum diffracted by the object will be redirected toward the CCD in such a way that, without the grating, they would fall outside the CCD aperture. Therefore, due to each additional frequency band diffracted by the grating arriving at the CCD with a different angle, its spectral content is recovered by inserting a reference beam in an off-axis [27,28] or in an on-axis [29] interferometric configuration. However, very modest resolution limits (above $15\,\mu m$) are experimentally validated using these approaches.

In a similar way, and according to the analogy between a diffraction grating and a set of tilted beams, the angular multiplexing of the input object spatial information can also be performed in digital holography by providing pulsed tilted illumination and coherence coding onto the input object [15]. In this case, a single laser pulse is split in amplitude into three subpulses, each one of them having a time delay with respect to the other two and each one of them being optically manipulated to achieve tilted beam illumination onto the input object. Later on, a single-frame CCD recording allows the recovery of the different multiplexed bands due to the coherence coding, and SA generation provides a superresolved image. However, this approach becomes difficult to assemble because of the rigorous optical beam path matching and also becomes restricted in the number of usable tilted beams, since the increase in the angular multiplexing directions implies complex procedures to split the original pulsed beam into additional ones. In addition, as the number of subpulses increases to multiplex more directions, the system becomes restricted in dynamic range, avoiding bandpass image recovery.

Now, the proposed approach presents a new procedure based on angular multiplexing provided by tilted beam illumination but having improved capabilities that allow the definition of a new resolution limit in the range of $1\,\mu m$. As it is depicted in Fig. 1(b), the illumination stage is composed of a prism that can be shifted and rotated to provide sequential oblique illumination onto the input object, thus, the shift allows tilted beam illumination at a given angle (defined by the deviation angle of the prism), and the rotation allows 2D spatial-frequency space coverage around a circle where the deviation angle of the prism is constant. Let us call this circle an illumination ring. Thus, once on-axis illumination is considered, the wedge prism is shifted to off-axis positions and rotated according to such positions in order to illuminate obliquely the input object. Figure 1(b) depicts one of those tilted beam illumina-

tion positions, while Fig. 2 illustrates the whole set of tilted illuminations where the object's diffracted wavefront has been divided into rectangular slots for clarity.

This illumination procedure permits the sequential recovery of different spectral bands of the object's spectrum when performing digital FT of every off-axis recorded hologram and a filtering process over one of the diffraction hologram orders. Thus, different rectangular elementary apertures [see Fig. 2] containing a different spatial-frequency range of the object's spectrum are recovered in time sequence. 2D Fourier space coverage is ensured by providing tilted beams around the illumination ring. This additional information can be properly managed to generate an SA, allowing superresolved imaging by a simple digital FT of the information contained in the SA.

Recovered elementary apertures must be contiguous in order to generate an SA having a synthetic cutoff frequency as high as possible. Otherwise, either if the illumination angle is too high there will be empty regions between apertures and the frequency space will not be fully covered, or if the illumination angle is too small there will be a great overlapping between apertures and the synthetic cutoff frequency will be low. Since the CCD is typically rectangular, the setup must be designed to provide contiguous elementary apertures in the shorter direction and, thus, overlapping in the larger one.
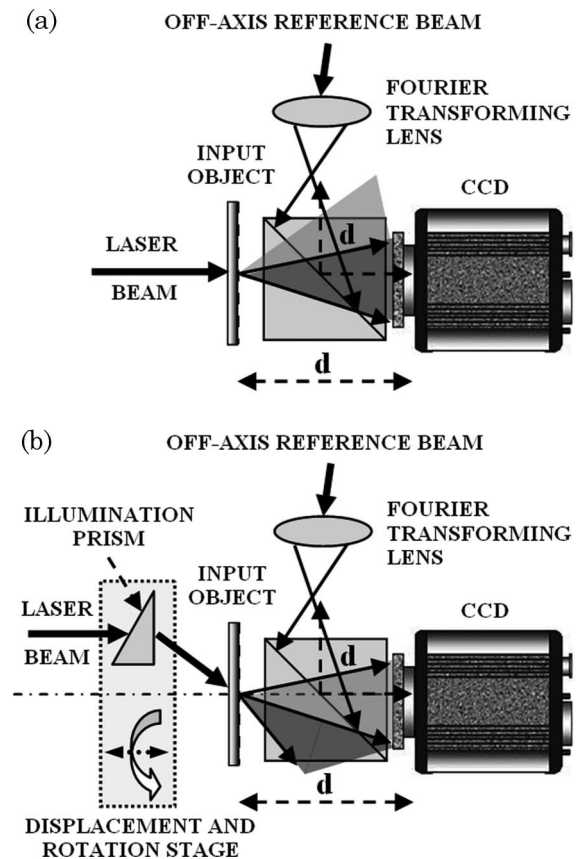

Fig. 1. Experimental setup arrangement for the proposed approach: (a) on-axis and (b) off-axis input object illumination cases.
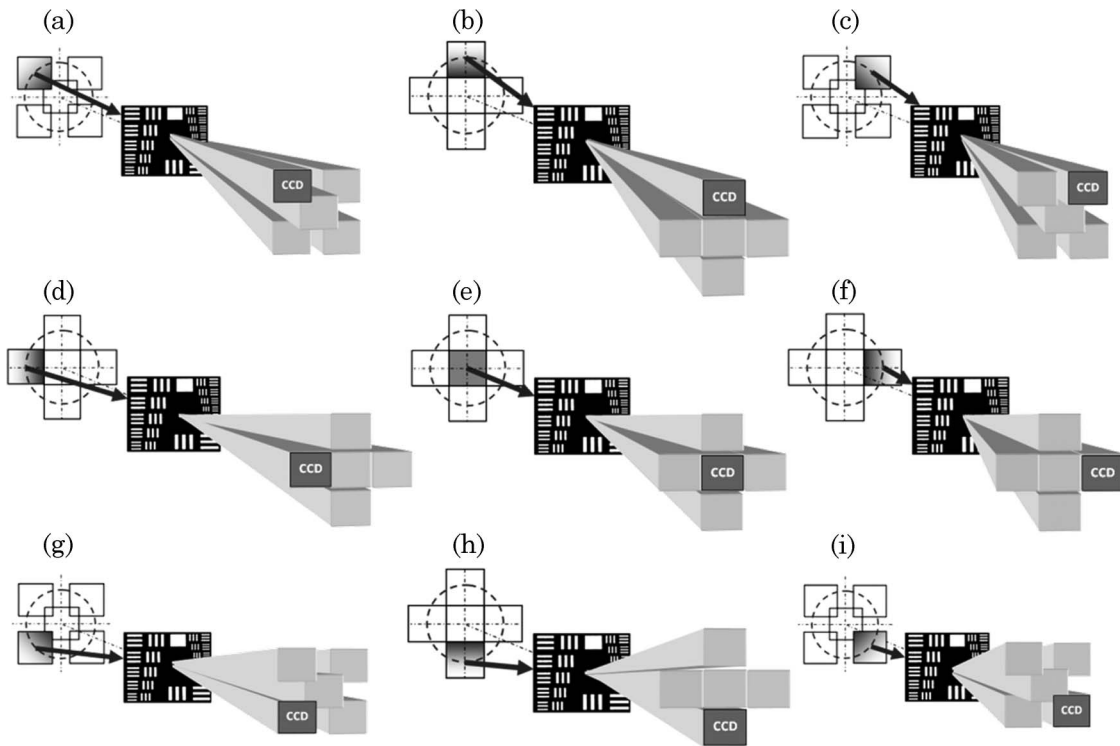
Fig. 2. Scheme of the angular multiplexing provided by tilted beam illumination in the proposed approach. From (a) to (i), different oblique beam directions allow the recording of different portions of the input object diffracted wavefront. The dashed circle represents the illumination ring where tilted beams are generated.

This fact can easily be fulfilled by either placing the CCD at a given distance from the input object so that the angle defined between the optical axis and the shorter CCD direction (typically the vertical one) will be half the oblique illumination angle, or selecting the deviation angle of the illumination prism to be twice the angle defined by the NA in the shorter CCD direction. In any case, a contiguous frequency band will be diffracted on axis when vertical tilted illumination impinges on the input object. Thus, the new vertical cutoff frequency is expanded three times or, equivalently, the resolution is improved by a factor of 3 in the vertical Fourier direction [21]. However, when applying the proposed method in other directions, the resolution gain will be slightly lower than 3 because the CCD is normally wider in the horizontal than in the vertical direction. Figure 3 depicts this situation.

Finally, the set of recovered bandpass images must be carefully managed to provide a high-quality reconstructed image. Typically, the position of each hologram in the Fourier domain is commanded by computing cross correlation between the overlapping areas in adjacent recordings [25]. As the overlapping increases, the reconstruction becomes more accurate but a higher number of recordings is needed. Recently, Jiang *et al.* reported a method to correctly overlap the different recordings in SA digital holography [37]. They used a procedure based on the maximization of both the reconstructed image quality using image variance criterion and the spectral energy distribution ratio between each pair of adjacent holograms obtained when the CCD is shifted. Here, we have adopted a similar strategy where three factors are considered in order to digitally synthesize a high-quality superresolved image. First, we have considered the addition of a global linear phase [$\exp(iC)$, C being a constant] to each recovered aperture coming from the different optical path traveled for each tilted illumination that is used in the illumination stage. Such an optical path difference is due to subwavelength distance mismatches that are impossible to match on each illumination separately. Second, we have considered that a difference in the divergence between both interference beams primarily introduces a misfocus in the reconstructed image. Aside from a fine adjustment of the distance "d" to be equal in both interferometric branches, small errors remain due to the FT lens in the reference branch. This effect will be the same for every hologram and can be compensated for by introducing a quadratic phase factor [$\exp(i2\pi(ax^2 + by^2)/\lambda)$, where (a, b) are coefficients proportional to the misfocus and λ is the illumination wavelength] in each recorded hologram [17,38]. Third, we have accurately replaced each recovered pupil to its original position at the object spectrum using the following steps. By knowing the oblique illumination angle, we have added a linear phase factor [$\exp(i2\pi(cx + dy)/\lambda)$, where (c, d) are coefficients proportional to the oblique illumination angle] to each recorded hologram in order to shift back each elementary aperture to a rough position in the Fourier domain. And final fine adjustment is accomplished by adding smaller linear
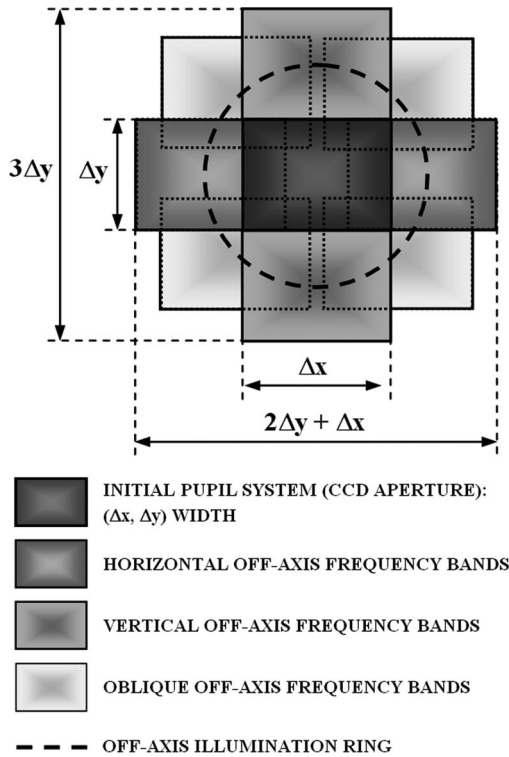
Fig. 3. Hypothetical SA for full 2D frequency space coverage generated by the addition of eight off-axis elementary apertures plus the on-axis one.

phase factors in both horizontal and vertical directions. This procedure is repeated for each elementary pupil used in the experiment. Although the whole process can be guided by an image quality criterion, as in [37], here the final reconstructed image is obtained by visual evaluation of the reconstructed image quality every time a new bandpass image is added to the others.

B. Theoretical System Analysis

In this subsection we present the mathematical foundation of the proposed approach. Having in mind the optical setup depicted in Fig. 1, the amplitude distribution arriving at the CCD plane comes from the addition of both an imaging and a reference beam. Assuming that collimated illumination impinges onto the input object, the imaging beam is obtained by Fresnel propagating the amplitude distribution at the input plane, which is given by

$$U_{\text{IP}}^{im}(x_0,y_0) = t(x_0,y_0) \exp\{j2\pi(\nu_m x_0 + \nu_n y_0)\}, \quad (1)$$

(x_0,y_0) being the spatial coordinates at the input plane, and $t(x_0,y_0)$ is the amplitude distribution of the input object. Note that the use of collimated illumination does not introduce any penalty in the setup. Moreover, it provides an advantage due to its simplicity and because it ensures beam power equalization in all illuminations.

The exponential factor in Eq. (1) gives an account of the illumination beam with a propagation carrier

frequency given by (ν_m,ν_n) in the horizontal and vertical directions, respectively. After propagation by a distance "d" in free space, the amplitude distribution arriving at the CCD from the imaging branch is

$$U_{\text{CCD}}^{im}(x,y) = C \exp\left\{j\frac{k}{2d}[x^2+y^2]\right\} \int \int t(x_0,y_0)$$
$$\times \exp\left\{j\frac{k}{2d}[x_0^2+y_0^2]\right\} \exp\left\{-j2\pi\left[\left(\frac{x}{\lambda d}-\nu_m\right)\right.\right.$$
$$\left.\left.\times x_0 + \left(\frac{y}{\lambda d}-\nu_n\right)y_0\right]\right\}\mathrm{d}x_0\mathrm{d}y_0, \quad (2)$$

k being the wavenumber, λ is the illumination wavelength, and C is a constant including all the constant factors. For convenience, let us rewrite Eq. (2) as

$$U_{\text{CCD}}^{im}(x,y) = C \exp\left\{j\frac{k}{2d}[x^2+y^2]\right\}\left[\text{FT}\{t(x_0,y_0)\}_{u',v'}\right.$$
$$\left.\otimes \text{FT}\left\{\exp\left\{j\frac{k}{2d}[x_0^2+y_0^2]\right\}\right\}_{u',v'}\right], \quad (3)$$

where $\otimes$ denotes convolution operation, and (u',v') are the scale factors of the FT defined as $u' = \frac{x}{\lambda d}-\nu_m$ and $v' = \frac{y}{\lambda d}-\nu_n$. Now, Eq. (3) is added, with the amplitude distribution incoming from the reference branch, that is, with an off-axis spherical reference beam diverging from the same distance "d" in front of the CCD in the form of

$$U_{\text{CCD}}^{\text{ref}}(x,y) = D \exp\left\{j\frac{k}{2d}\left[(x-x_r)^2+(y-y_r)^2\right]\right\}, \quad (4)$$

where D is the amplitude of the reference beam and (x_r,y_r) is the off-axis point where the reference beam is generated. Thus, the total amplitude distribution at the CCD plane comes from the addition of Eqs. (3) and (4) multiplied by the CCD rectangular shape that trims the recording area at the output plane. And finally, the CCD performs an intensity operation over the total amplitude

$$I_{\text{CCD}}^{\text{total}}(x,y) = |U_{\text{CCD}}^{\text{total}}(x,y)|^2 = \left|[U_{\text{CCD}}^{im}(x,y)\right.$$
$$+ U_{\text{CCD}}^{\text{ref}}(x,y)]\text{rect}\left(\frac{x}{\Delta x},\frac{y}{\Delta y}\right)\bigg|^2$$
$$= [|U_{\text{CCD}}^{im}|^2 + |U_{\text{CCD}}^{\text{ref}}|^2 + U_{\text{CCD}}^{im}U_{\text{CCD}}^{\text{ref}*}$$
$$+ U_{\text{CCD}}^{im*}U_{\text{CCD}}^{\text{ref}}]\text{rect}\left(\frac{x}{\Delta x},\frac{y}{\Delta y}\right), \quad (5)$$

where $*$ represents the complex conjugate and $(\Delta x,\Delta y)$ are the width of the CCD sensing area in the horizontal and vertical directions, respectively, which can be defined under paraxial approximation as $\Delta x = 2d\text{NA}_{\text{HOR}}$ and $\Delta y = 2d\text{NA}_{\text{VER}}$, NA_{HOR} and NA_{VER} being the NA values of the imaging system in the horizontal and vertical directions, respectively.

Since the proposed approach is based on a digital lensless Fourier holographic configuration, we must perform the FT operation of Eq. (5) in order to get imaging. But this procedure provides four terms that can be separately analyzed. The first one is the auto-correlation slot of the diffracted object wavefront selected by the considered tilted beam

$$
\begin{aligned}
T_1(u,v) = \mathrm{FT}&\left\{ |U_{\mathrm{CCD}}^{im}|^2 \mathrm{rect}\left(\frac{x}{\Delta x}, \frac{y}{\Delta y}\right) \right\} = \mathrm{FT}\{U_{\mathrm{CCD}}^{im}\} \\
&\otimes \mathrm{FT}\{U_{\mathrm{CCD}}^{im\,*}\} \\
&\otimes \mathrm{FT}\left\{ \mathrm{rect}\left(\frac{x}{\Delta x}, \frac{y}{\Delta y}\right) \right\},
\end{aligned}
\tag{6}
$$

(u,v) being the spatial-frequency coordinates. Since this term is not dependent on the reference beam, it will be centered at the Fourier domain. Something similar happens with the second term $T_2(u,v)$ that comes from the FT of the square modulus amplitude distribution provided by the reference beam multiplied by the *rect* function representative of the CCD. So, $T_2(u,v)$ implies the convolution of a delta function with the FT of the CCD aperture that is centered at the origin. Since the carrier frequency between both interferometric beams can be easily adjusted by slightly tilting the off-axis reference beam in the experimental setup, the hologram orders will not overlap with the zero order term. Thus, we can put aside in our analysis these two terms since they define the zero hologram order. Thus, the third term allows the recovery of the complex amplitude distribution of the frequency bandpass selected by the illumination beam

$$
\begin{aligned}
T_3(u,v) = \mathrm{FT}&\left\{ U_{\mathrm{CCD}}^{im} U_{\mathrm{CCD}}^{\mathrm{ref}\,*} \mathrm{rect}\left(\frac{x}{\Delta x}, \frac{y}{\Delta y}\right) \right\} \\
= \mathrm{FT}&\left\{ C'\left[\tilde{t}\left(\frac{x}{\lambda d} - \nu_m, \frac{y}{\lambda d} - \nu_n \right) \right.\right. \\
&\otimes \mathrm{FT}\left\{ \left.\left. \exp\left\{ j\frac{k}{2d}[x_0^2 + y_0^2] \right\} \right\}_{u',v'} \right] \right\}, \\
&\otimes \mathrm{FT}\left\{ \exp\left\{ j\frac{2\pi}{\lambda d}[x_r x + y_r y] \right\} \right\} \\
&\otimes \mathrm{FT}\left\{ \mathrm{rect}\left(\frac{x}{\Delta x}, \frac{y}{\Delta y}\right) \right\} = C'\left\{ [t(\lambda d x, \lambda d y) \right. \\
&\times \exp\{j2\pi(\nu_m x + \nu_n y)\}] \\
&\times \exp\left\{ j\frac{k}{2d'}(x_0^2 + y_0^2) \right\} \right\} \\
&\otimes \mathrm{FT}\left\{ \mathrm{rect}\left(\frac{x}{\Delta x}, \frac{y}{\Delta y}\right) \right\} \\
&\otimes \delta\left(u - \frac{x_r}{\lambda d}, v - \frac{y_r}{\lambda d} \right)
\end{aligned}
\tag{7}
$$

C' being the redefined global constant and d' is the new distance of the divergent illumination beam incoming from the double FT process. Note that the fourth term from Eq. (5) is the complex conjugate

of the third term and has an equivalent meaning to it.

But now we must carefully analyze the different terms in Eq. (7). Taking a look at the square bracket, we can see that a scaled version of the complex amplitude distribution of the input object is multiplied by a linear phase factor coming from the illumination beam. That is, depending on the tilted beam we choose in the illumination procedure, a different spectral content of the input object spectrum will be accessible at the Fourier domain. This bandpass image is multiplied by a quadratic phase factor related with the axial point of the input plane and representative of the imaging beam divergence. After that, a convolution with the FT of the CCD rectangular area represents the limitation in the spatial-frequency content of the transmitted bandpass image due to the CCD aperture. And finally, the resulting spectral distribution is moved away from the center of the Fourier domain by the convolution with the delta function incoming from the off-axis reference beam. Notice that the action of the reference beam, aside from avoiding the overlap of the different hologram orders, is to cancel the quadratic phase factor outside the square bracket in Eq. (3) in such a way that the bandpass image of the input object selected by the tilted beam becomes imaged at the Fourier domain. The carrier frequency in the holographic recording can be properly tuned by rotating the beam splitter cube.

So, depending on the tilted beam defined by (ν_m, ν_n), a different bandpass image of the input object having different spectral content can be recovered in time sequence. Finally, by time multiplexing the whole 2D frequency space, a set of different elementary pupils is recovered and used to synthesize an SA, expanding the cutoff frequency of the imaging system by proper relocation of each elementary aperture to its original position at the object's spectrum. This procedure is performed in a latter digital processing stage that finally culminates in a superresolved image of the input object, by FT, the spectral information contained in the generated SA.

3. Experimental Results

In this section we include the optical experimental validation of the proposed approach, considered in two subsections. In the first one, initial calibration of the system setup is presented as a way to both adjust the experimental setup and provide a first shape of SA. Resolution limits, as well as NA and synthetic numerical aperture (SNA) values, are theoretically provided and experimentally validated. Once the experimental setup is properly adjusted, the second subsection shows different shapes of SA, depending on the disposable *a priori* information about the input object. In all the cases, we use an He–Ne laser (632 nm emitting wavelength) as an illumination source, a CCD (Basler A312f, 582×782 pixels, $8.3\,\mu\mathrm{m}$ pixel size, 12 bits/pixel) as an imaging device, a wedge prism with 10 deg deviation angle as the

illumination prism, a beam splitter cube (20 mm× 20 mm side, BK7) to allow holographic recording, and a doublet lens (80 mm focal length and 60 mm diameter) to provide a spherical divergent off-axis reference beam. Optic mounts, beam expanders, neutral density filter wheels to equalize the beam aspect ratio, and micrometric translation stages complete the experimental setup.

A. System Calibration

In order to calibrate the experimental setup, we use a negative high-resolution United States Air Force (USAF) test target as the input object. The test target is placed 36 mm in front of the CCD, but the presence of a beam splitter cube brings its image through, closer to the CCD [39]. Under paraxial approximation, the displacement Δs originated by a plano–parallel plate is given by $\Delta s = e(1 - 1/n)$, where e and n are the width and the refractive index of the plate, respectively. According to technical specifications provided by Schott [40], the refractive index of BK7 at the He–Ne wavelength is 1.515, and then the displacement introduced by the beam splitter cube is around $\Delta s = 6.6$ mm. Thus, the effective distance between the test target and the CCD is 29.4 mm. Obviously, the reference beam is also forced to diverge from a distance equal to 29.4 mm in front of the CCD in order to get imaging at the Fourier domain [see Fig. 1]. The distance in the reference branch can be easily tuned by computing on-line digital FT of the recorded hologram until the test target will appear focused at the Fourier domain.

Using this effective distance and the theoretical specifications of the CCD, the NAs and the resolution limits in the horizontal and vertical directions are $\mathrm{NA_{HOR}} = 0.11$ and $\mathrm{NA_{VER}} = 0.08$, and $R_{\mathrm{HOR}} = 5.74\,\mu\mathrm{m}$ (174 lp/mm) and $R_{\mathrm{VER}} = 7.72\,\mu\mathrm{m}$ (130 lp/mm), respectively, where lp is line pairs. Figure 4 depicts the FT of the recorded hologram when on-axis illumination is used [case (a)] and the magnified region of interest [case (b)]. Note that the bandpass of the system is neatly inside the discrete FT of the image. This implies that the Nyquist criterion for sampling is fulfilled, or, in other words, the pixel size in the sensor is smaller than the spatial detail of the recorded intensity [41,42]. We can see as the smallest resolved details have a size of 161 lp/mm (group 7, element 3—named G7-E3 as a convention from now on) and 128 lp/mm (G7-E1) in horizontal (vertical bars) and vertical (horizontal bars), respectively. Although these values are a little bit lower than theoretical ones, they are in good concordance with the theoretical values, since the following element in the resolution test is below the diffraction limit (G7-E4 and G7-E2 have a detail size of 181 lp/mm and 144 lp/mm, respectively). Additionally, the illuminated object field of view must be limited [15,27–29]. Otherwise, the twin image should affect the real image, and vice versa. In our case, we have used a 2D square aperture to limit the extension of the illumination beam at the input plane.

Then we perform the proposed superresolution approach. The illumination prism is placed in a translation and rotatable stage, and it is shifted and rotated to the off-axis positions. Also, the double slit is moved together with the prism to maintain the field of view limitation. To provide tilted beam illumination, the incident laser beam is expanded by using a pinhole in combination with a collimation lens. Thus, incident laser light is obtained over the whole set of off-axis positions where the illumination prism is moved.

Since we know that the USAF test target is mainly composed of horizontal and vertical lines, we only consider off-axis illuminations in such orthogonal directions. Just as an example, Fig. 5 shows the FT of two recorded holograms when using horizontal [case (a)] and vertical [case (d)] off-axis illuminations as well as the four bandpass images of the region of
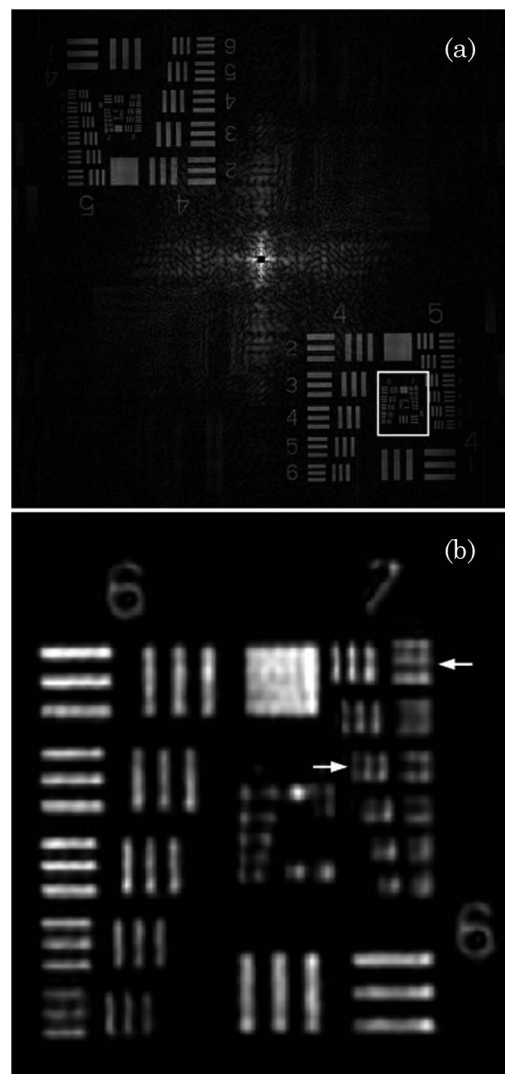

Fig. 4. (a) FT of the recorded hologram and (b) magnified area (inner part of the USAF test) marked with the solid white line in (a). DC term in (a) has been blocked to enhance image contrast, and white arrows in (b) mark the resolution limits in the vertical and horizontal directions.

interest (inner part of the USAF test) corresponding with the four tilted beam illuminations [magnified images inside cases (a) and (b), and cases (c) and (d)].

Once each bandpass image is recovered by filtering at the Fourier domain, they are used to assemble an SA by coherent addition of the different bandpass images. Figure 6 depicts the SA [case (a)] and the superresolved image [case (b)] obtained by FT of the SA. In accord with the theoretical prediction, the SNA and the superresolution limits in horizontal and in vertical are given by $SNA_{HOR} = NA_{HOR} + NA_{ILUM} = 0.28$ and $SNA_{VER} = NA_{VER} + NA_{ILUM} = 0.25$, and $SR_{HOR} = 2.26\,\mu m$ (442 lp/mm) and $SR_{VER} = 2.53\,\mu m$ (395 lp/mm), respectively, NA_{ILUM} being the NA of the illumination and SR the new superresolution limit. From Fig. 6(b), we can see that the last resolved elements are G8-E5 (406 lp/mm) and G8-E4 (362 lp/mm) in horizontal and vertical directions, respectively. Once again, these experimental values agree with the theoretical prediction since the following elements in the USAF test are below the superresolved diffraction limit: G8-E6 (456 lp/mm) and G8-E5 (406 lp/mm) for horizontal and vertical directions. In this case, the gain factors in the resolution are 2.5 and 3 when comparing the resolution limits in both horizontal and vertical directions, respectively, without and with the proposed approach.

B. Synthetic Aperture Shaping

In this subsection we show the capabilities of the proposed approach for easily synthesizing any SA shape and the adaptation of the generated SA to the type of imaged object. As the first case, we report on the possibility that the input object contains the quasi-totality of useful information in orthogonal directions at the Fourier domain but not in the vertical and horizontal ones. To demonstrate this particular case, we consider a 45 deg rotation of the USAF test at the input plane. Figures 7(a) and 7(b) show the case when off-axis oblique illumination at 45 deg is used (FT of the recorded hologram and magnified area of interest, respectively). Analogously, cases (c) and (d) correspond with the case of 135 deg off-axis oblique illumination.

In these conditions and under on-axis illumination, the CCD defines the same NA for the two orthogonal directions. Making some simple calculations, the new NA is equal to 0.115 in both directions and the new resolution limit is $5.5\,\mu m$ (181 lp/mm). We can see that the last resolved element is now G7-E3 (161 lp/mm) in both directions [see white arrows in Fig. 7(e)]. Although G7-E4 (181 lp/mm) coincides exactly with the theoretical resolution limit, this element does not appear resolved in the image because it is in the limit of the imaging setup resolution. Then SA generation is performed using tilted beam illumination only in the oblique orthogonal directions, that is, 45-135-225-315 deg illumination directions. As a final result, four off-axis rectangular apertures are recovered and used to assemble the SA by coherent
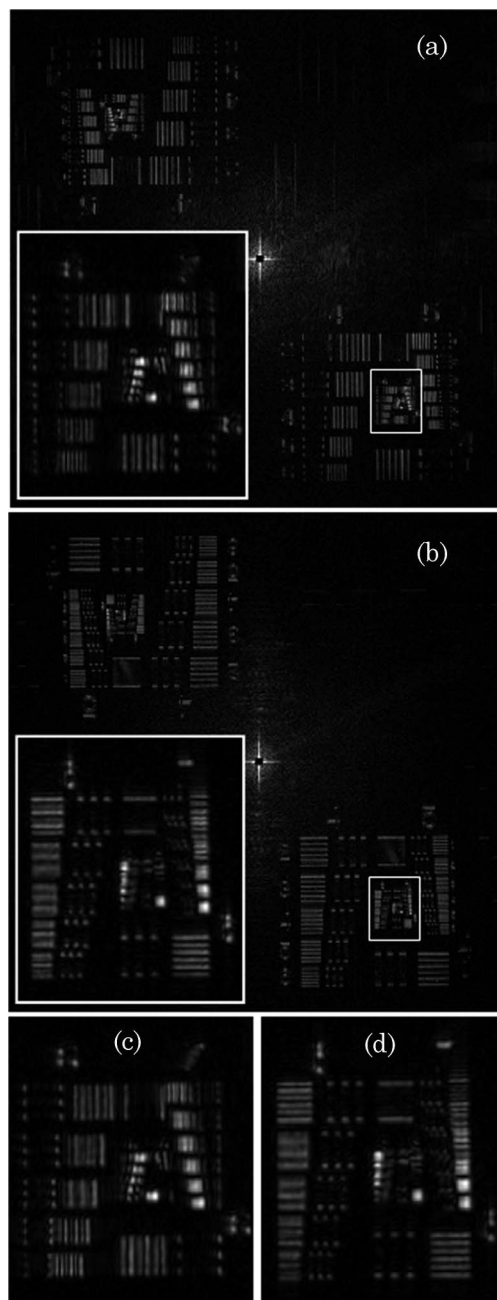

Fig. 5. (a) and (b) are the FT of the recorded holograms for horizontal (right) and vertical (up) off-axis illuminations, respectively. Inner images magnify the area of interest (solid white rectangle). (c) and (d) correspond with the area of interest when considering the complementary horizontal (left) and vertical (down) off-axis illuminations.

addition with the on-axis one [Fig. 7(f)]. No special care (attenuation of the overlapping area) has been taken when adding overlapping spectrums at the Fourier domain. The superresolved image is depicted in Fig. 7(g). Now the resolution limit is experimentally improved until G8-E5 (406 lp/mm), and its corresponding theoretical value comes from an SNA value equal to $SNA = NA_{CCD} + NA_{ILUM} = 0.285$ that defines a superresolution limit equal to $SR = 2.22\,\mu m$ (450 lp/mm). Note that those values are
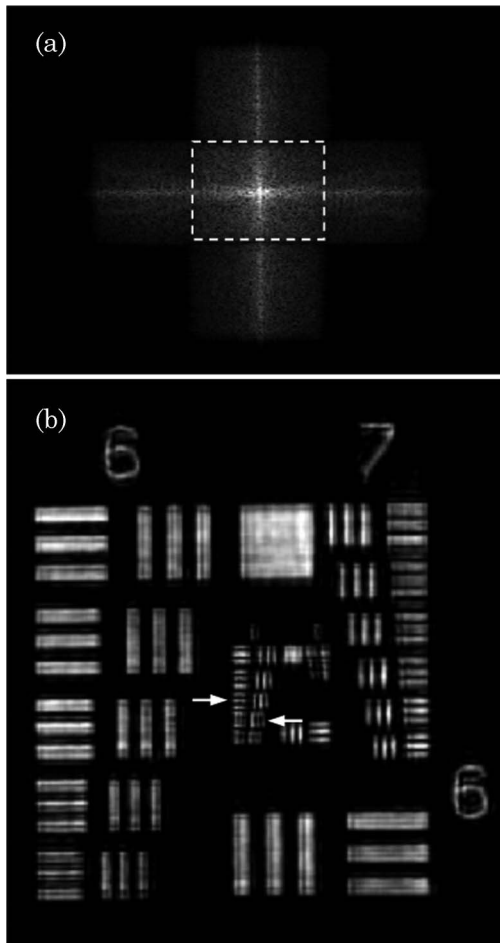
Fig. 6. (a) generated SA where the conventional aperture is shown with a dashed white line and (b) superresolved image.

the same for both superresolved directions. Once again, both experimental and theoretical values are in good agreement, since the following USAF element (G8-E6) is below the superresolved diffraction limit (456 lp/mm).

As a second case, we present the general case where the input object contains information in every direction at the spatial-frequency space. Then SA generation must cover the whole spatial-frequency plane by considering the addition of elementary apertures in all possible directions (0-45-90-135-180-225-270-315 deg tilted illuminations). To illustrate this case, we present experimental results obtained when using a biosample of fixed human red blood cells. The erythrocyte slide is stained using a specially prepared mixture of Methylene Blue and Eosin in methanol (Wright's stain). Now the theoretical values defined by the experimental setup are those presented in Subsection 3.A ($NA_{HOR} = 0.11$ and $NA_{VER} = 0.08$, and $R_{HOR} = 5.74\,\mu m$ and $R_{VER} = 7.72\,\mu m$). Figures 8(a)–8(d) show the cases when on-axis and horizontal, vertical, and oblique (45 deg) off-axis illumination, respectively, are used. Insets depict magnified images of the area of interest on each case. The lower inset in case (a) defines

the low-resolution image provided by the conventional imaging mode. This low-resolution image is also depicted in case (f), where we can see that the image presents higher resolution in the horizontal than in the vertical direction, in accord with the rectangular size of the CCD. Moreover, since the red blood cells are around 6–$7\,\mu m$ in diameter, they are not imaged in the vertical direction but can be barely seen in the limit for the horizontal direction. After performing the proposed approach, Fig. 8(e) depicts the SA generated by coherent addition of the eight off-axis rectangular pupils, where the conventional rectangular aperture is again marked with a dashed white rectangle for clarity. Once again, no attenuation of the overlapping area when adding the different spectrums is considered. And finally, the superresolved image is presented in Fig. 8(g), showing the resolution improvement. Notice that, in some cells, there appears a faint black point in the center. This black point is originated by deviation of the light at the center of the cells due to the typical donutlike shape of the red blood cells. According to the theory, the SNA values and the new resolution limits are those presented in the USAF validation ($SNA_{HOR} = 0.28$, $SNA_{VER} = 0.25$, $SNA_{OBLIQUE} = 0.285$, and $SR_{HOR} = 2.26\,\mu m$, $SR_{VER} = 2.53\,\mu m$ and $SR_{OBLIQUE} = 2.22\,\mu m$), values that enable image formation of the cells.

Finally, and as a third case, we show now how to further improve the resolution limit while performing the proposed approach. By considering a second illumination ring at twice the oblique illumination angle of the first ring, it is possible to expand up the synthetic cutoff frequency by addition of a new rectangular pupil. This second illumination ring can be produced by both the use of a new wedge prism having a deviation angle twice the angle of the prism used in the previous experiments, that is, 20 deg, or a combination of two identical wedgelike prisms in a beam steering application. We have selected the second option, where two identical prisms having a 10 deg deviation angle are combined. Notice that the paraxial condition supposed in the analysis of the beam splitter cube still prevails because each recording defines an NA of 0.1, independently of the illumination angle. Thus, the first illumination ring is provided by a single prism covering the four orthogonal directions of the USAF target, and then a second illumination ring is performed using the two prisms together. With this procedure, a set of tilted beams having an oblique illumination angle of 20 deg can be produced over the input plane: this is our second illumination ring.

To experimentally validate that it is possible to further achieve a better resolution limit, we use the USAF test target as the input object. Once again, the NAs and the resolution limits in the horizontal and vertical directions of the imaging system with on-axis illumination are those ones specified in Subsection 3.A. Since we want to show proof of principle validation, and the USAF test has the most useful
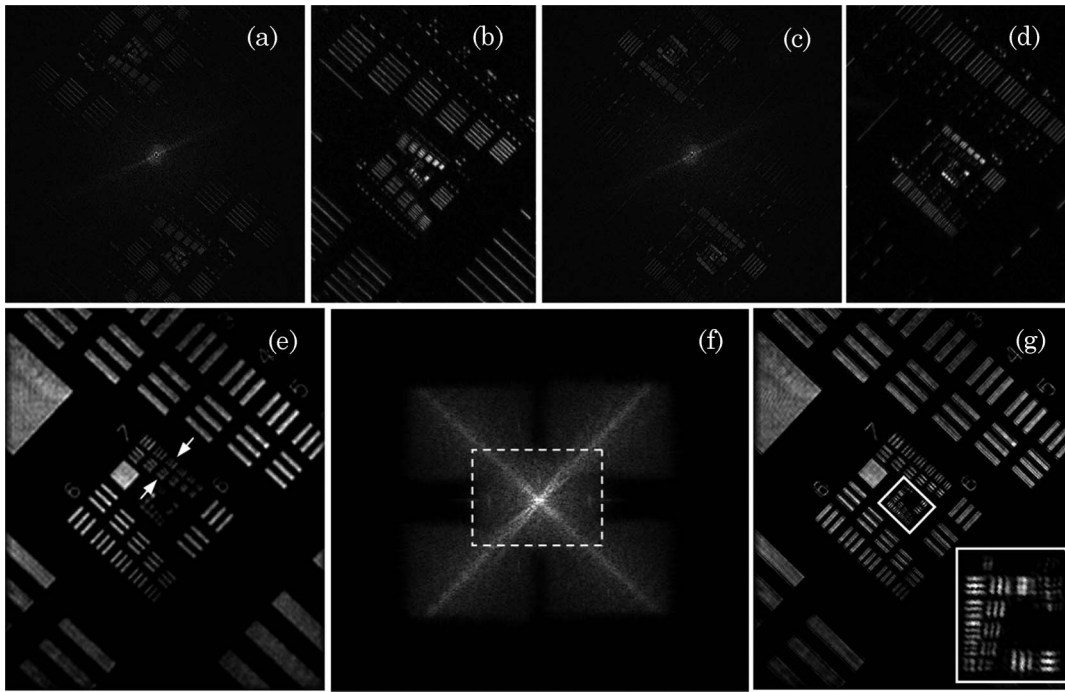
Fig. 7. USAF test rotated 45 deg: (a)–(b) are the FT of the recorded hologram when off-axis oblique (45 deg) illumination is used and a magnification of the area of interest, respectively. (c)–(d) are the equivalent images when off-axis oblique (135 deg) illumination is considered. (e) is the low-resolution image magnification obtained with on-axis illumination, (f) is the generated SA (the conventional aperture is marked with a dashed white rectangle), and (g) is the superresolved image.
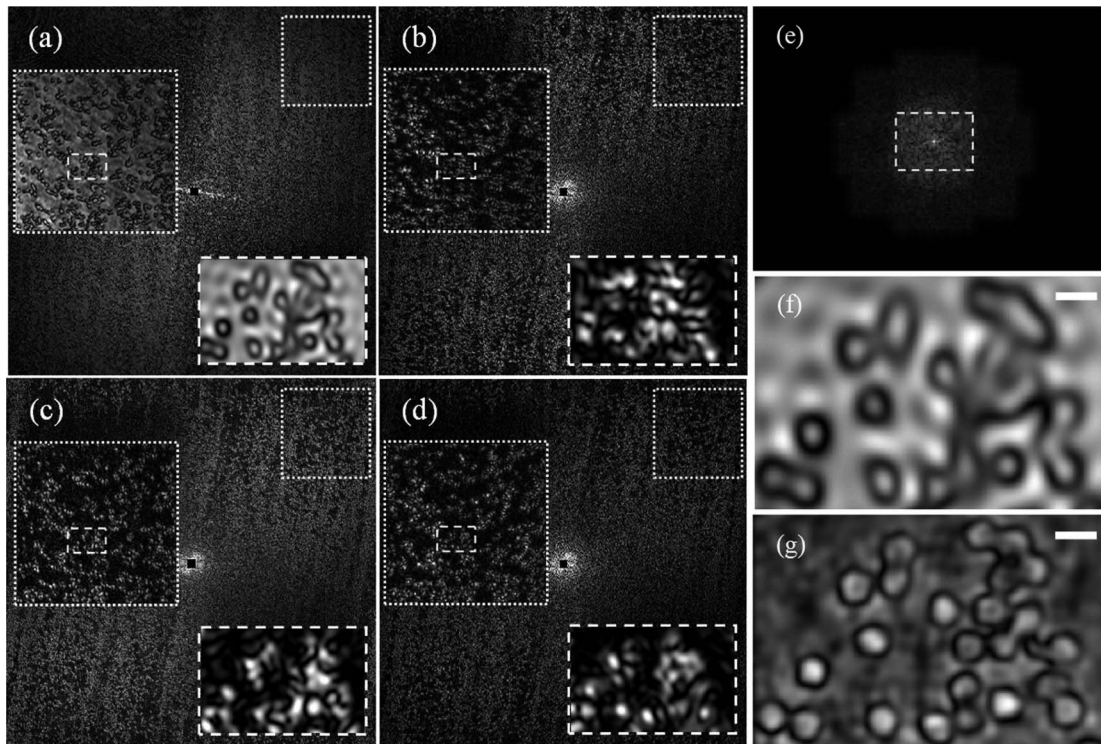

Fig. 8. Cell biosample case: (a) FT of the recorded hologram when on-axis illumination is considered. The inner figures marked with dotted and dashed white lines show increasing magnification of the area of interest. (b)–(d) are the equivalent images when horizontal, vertical, and oblique illuminations are used, respectively. (e) is the generated SA (the conventional aperture is marked with a dashed white rectangle). (f) is the conventional imaging mode when on-axis illumination is considered. (g) is the superresolved image. The white scale bars in the upper-right corner of (f) and (g) are $10\,\mu\mathrm{m}$.

spatial-frequency information in vertical and horizontal orthogonal directions, four tilted beams are considered for both the first and second illumination rings. Figures 9(a)–9(d) depict the cases when horizontal off-axis illuminations coming from the first and second illumination rings, respectively, are considered. Vertical off-axis illuminations are shown in cases 9(e)–9(h). The low-resolution image obtained by using on-axis illumination is depicted in Fig. 9(i).

Once the whole illumination procedure is performed, the different off-axis elementary apertures are recovered and used to synthesize the expanded SA [Fig. 9(j)]. And the superresolved image is, again obtained by FT, the spectral information contained in the SA [Fig. 9(k)].

In addition, Fig. 10 depicts the inner parts of the images presented in Figs. 9(j) and 9(k) to clearly show the new improved image. Also, Fig. 10(c) plots a vertical cross section, comparing the three elements that integrate group number 9 of the USAF test. We can see that the three bars of the three elements are resolved in both the superresolved image and the solid-line plot. According to the theory, the SNA and the superresolution limits in horizontal and vertical are given by $SNA_{HOR} = 0.45$ and $SNA_{VER} = 0.42$, and $SR_{HOR} = 1.41\,\mu m$ (709 lp/mm) and $SR_{VER} = 1.51\,\mu m$ (664 lp/mm), respectively, taken into account that now the NA of the illumination is 0.34, corresponding with the second illumination ring. These values are good enough to resolve the last element of the USAF test defined by G9-E3 (645 lp/mm). With these new values, the gain factors in resolution are around 4 and 5 when comparing with the conventional imaging mode.

4. Conclusions and Discussion

We have presented a step forward in imaging through digital lensless Fourier holography by reporting on a method capable of improving the image resolution in such a system configuration that is based on SA generation. The different shapes of SA are generated by using time-multiplexing tilted illumination onto the input object and *a priori* knowledge about the imaged object. Thus, customized SA shaping by coherent addition of elementary apertures only in the directions of interest (those directions where the object presents useful spatial-frequency information) is demonstrated for two different
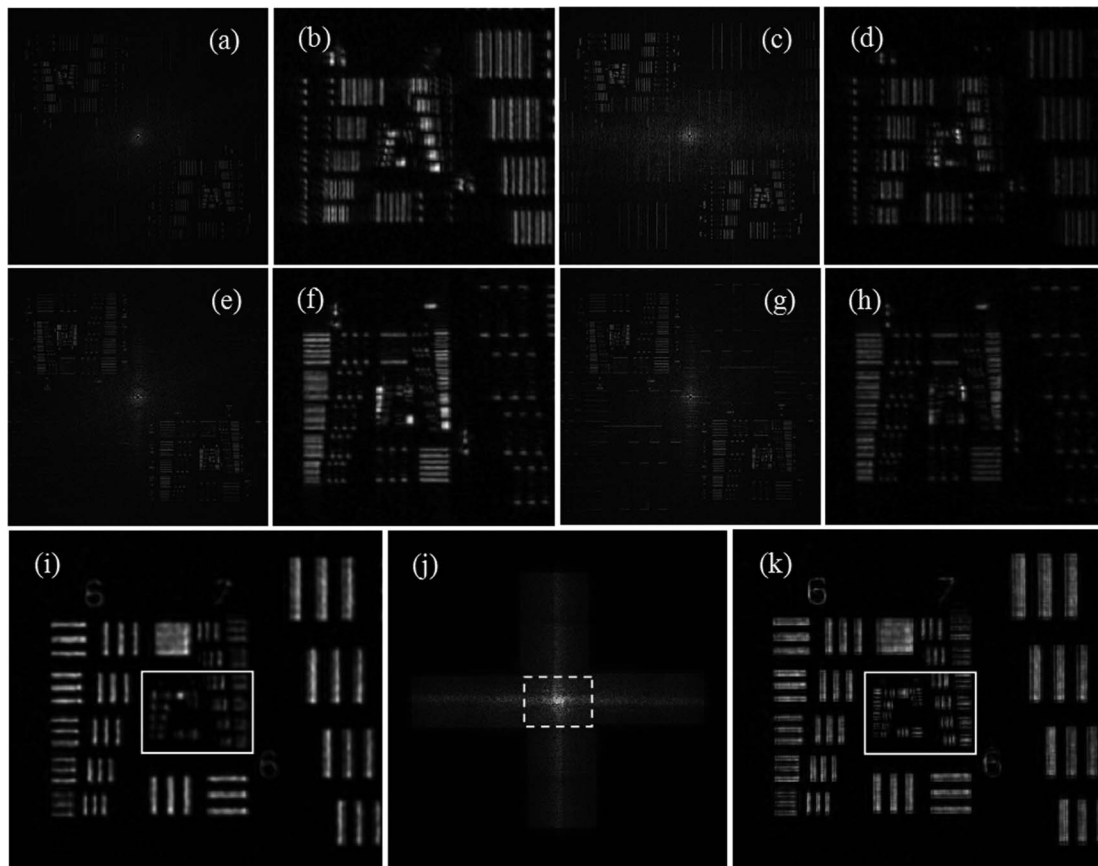

Fig. 9. USAF test and second illumination ring: (a)–(b) are the FT of the recorded hologram when horizontal off-axis illumination of the first illumination ring is considered and a magnification over the area of interest, respectively. (c)–(d) are the equivalent images when horizontal off-axis illumination of the second illumination ring is used. (e)–(f) and (g)–(h) are the equivalent images for the first and second illumination rings, respectively, when considering vertical off-axis illumination. Finally, (i) is the conventional image provided by on-axis illumination, (j) is the generated SA considering the addition of eight off-axis apertures alongside the conventional one (marked with a dashed white rectangle), and (k) is the superresolved image.
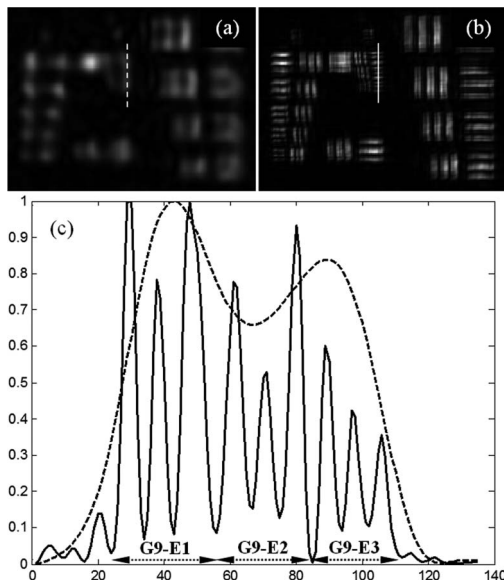
Fig. 10. (a) and (b) are magnified areas of the inner parts marked with a solid white line rectangle in cases (a) and (c) of Fig. 9, respectively. (c) plots the vertical cross sections corresponding with the lines in cases (a) and (b). The dashed curve represents the conventional image, and the solid curve is representative of the super-resolved image case.

objects: a synthetic resolution test and a complex cells sample. The proposed approach can be easily adapted to any system requirements, that is, it means a versatile, simple and customized method to improve resolution in digital lensless Fourier holographic microscopy imaging. Finally, theoretical calculations and experimental validation are presented, showing a good concordance between them.

Other lensless approaches allowing the generation of an SA by means of time-multiplexing tilted beam illumination in digital holography have been reported [14,16]. The main novelty is that the recording pattern is not in the spatial domain (FT of the given frequency band) but in the Fourier space (image of a frequency bandpass). This fact increases the system information capacity for a given camera, but also can lead to ambiguity of phase determination and possible information loss for patterns with high periodicity due to a restricted detection dynamic range. The authors have demonstrated an SNA close to 0.75 coming from the addition of multiple off-axis holograms, where each individual one has a rectangular equivalent extension of 0.13 NA. However, the generated SA does not imply full 2D coverage of the object's spectrum (four noncontiguous rectangular areas due to the CCD aperture shape in [14] and an annular shape aperture in [16]). Thus, the synthesized images resemble those obtained when using dark-field coherent microscopy. In that case, *a priori* knowledge about the input object is known and used to define the angle of the illumination beam. In a similar way, we use *a priori* information about the input object to multiplex only the directions of interest,

but here it is simpler to cover the full 2D object spectrum when generating the SA.

Moreover, we have experimentally demonstrated the versatility of the method to generate different SA shapes, not only for synthetic resolution test objects but also for more complex samples such as human red blood cells. Because of that, and due to the holographic nature of the method, phase visualization and quantification can be achieved for those samples where phase information will be much more relevant than the amplitude one. Thus, the combination of the proposed method with digital image processing enables a lot of capabilities for phase sample imaging, such as phase contrast or differential interference contrast imaging [31], three-dimensional sample representation [22], or even refocusing the sample at different planes [23].

In addition, the proposed method demonstrates a gain in resolution of 3 providing an improved resolution limit of around $2.2\,\mu$m (best value) while covering the whole 2D spatial-frequency space. The possibility to achieve better values is also reported by adding more external elementary apertures using a second illumination ring coming from the combination of two prisms in the illumination procedure. With this second illumination ring, the SNA, super-resolution limit, and resolution gain best values are 0.45, $1.41\,\mu$m, and 5, respectively. This is the first time, to the best of our knowledge, that such values are reported in digital lensless Fourier holography. Other digital lensless Fourier holographic superresolution methods are based on diffraction gratings [27,28] or tilted pulsed beam illumination [15] and have the advantage of being able to work in a single illumination shot because their underlying principle is spatial rather than time multiplexing. However, those methods demonstrated more modest improvements in comparison with the one reported here. Just as an example, [28] demonstrates a resolution gain factor of 1.6 with a resolution limit of $20\,\mu$m, while [15] reported on a gain in resolution of 1.78, arriving until $6.5\,\mu$m of resolution limit, approximately. Now, we have reached a resolution limit of around $1.4\,\mu$m, enabling the proposed method for real microscopic applications.

References

1. E. Abbe, "Beitrage zür theorie des mikroskops und der mikroskopischen wahrnehmung," Archiv. Microskopische Anat. **9**, 413–468 (1873).
2. M. Françon, "Amélioration de resolution d'optique," Nuovo Cimento Suppl. **9**, 283–290 (1952).
3. G. Toraldo di Francia, "Resolving power and information," J. Opt. Soc. Am. **45**, 497–501 (1955).

4. I. J. Cox and C. J. R. Sheppard, "Information capacity and resolution in an optical system," J. Opt. Soc. Am. A **3**, 1152–1158 (1986).

5. W. Lukosz, "Optical systems with resolving powers exceeding the classical limit," J. Opt. Soc. Am. **56**, 1463–1472 (1966).

6. W. Lukosz, "Optical systems with resolving powers exceeding the classical limit II," J. Opt. Soc. Am. **57**, 932–941 (1967).

7. Z. Zalevsky and D. Mendlovic, *Optical Super Resolution* (Springer, 2002).

8. X. Chen and S. R. J. Brueck, "Imaging interferometric lithography: approaching the resolution limits of optics," Opt. Lett. **24**, 124–126 (1999).

9. C. J. Schwarz, Y. Kuznetsova, and S. R. J. Brueck, "Imaging interferometric microscopy," Opt. Lett. **28**, 1424–1426 (2003).

10. V. Mico, Z. Zalevsky, P. García-Martínez, and J. García, "Single step superresolution by interferometric imaging," Opt. Express **12**, 2589–2596 (2004).

11. M. Ueda and T. Sato, "Superresolution by holography," J. Opt. Soc. Am. **61**, 418–419 (1971).

12. M. Ueda, T. Sato, and M. Kondo, "Superresolution by multiple superposition of image holograms having different carrier frequencies," Opt. Acta **20**, 403–410 (1973).

13. T. Sato, M. Ueda, and G. Yamagishi, "Superresolution microscope using electrical superposition of holograms," Appl. Opt. **13**, 406–408 (1974).

14. S. A. Alexandrov, T. R. Hillman, T. Gutzler, and D. D. Sampson, "Synthetic aperture Fourier holographic optical microscopy," Phys. Rev. Lett. **97**, 168102 (2006).

15. C. Yuan, H. Zhai, and H. Liu, "Angular multiplexing in pulsed digital holography for aperture synthesis," Opt. Lett. **33**, 2356–2358 (2008).

16. T. R. Hillman, T. Gutzler, S. A. Alexandrov, and D. D. Sampson, "High-resolution, wide-field object reconstruction with synthetic aperture Fourier holographic optical microscopy," Opt. Express **17**, 7873–7892 (2009).

17. V. Mico, Z. Zalevsky, P. García-Martínez, and J. García, "Superresolved imaging in digital holography by superposition of tilted wavefronts," Appl. Opt. **45**, 822–828 (2006).

18. V. Mico, Z. Zalevsky, and J. García, "Superresolution optical system by common-path interferometry," Opt. Express **14**, 5168–5177 (2006).

19. G. Indebetouw, Y. Tada, J. Rosen, and G. Brooker, "Scanning holographic microscopy with resolution exceeding the Rayleigh limit of the objective by superposition of off-axis holograms," Appl. Opt. **46**, 993–1000 (2007).

20. Y. Kuznetsova, A. Neumann, and S. R. J. Brueck, "Imaging interferometric microscopy—approaching the linear system limits of optical resolution," Opt. Express **15**, 6651–6663 (2007).

21. V. Mico, Z. Zalevsky, and J. García, "Synthetic aperture microscopy using off-axis illumination and polarization coding," Opt. Commun. **276**, 209–217 (2007).

22. V. Mico, Z. Zalevsky, and J. García, "Common-path phase-shifting digital holographic microscopy: a way to quantitative imaging and superresolution," Opt. Commun. **281**, 4273–4281 (2008).

23. V. Mico, Z. Zalevsky, C. Ferreira, and J. García, "Superresolution digital holographic microscopy for three-dimensional samples," Opt. Express **16**, 19260–19270 (2008).

24. F. Le Clerc, M. Gross, and L. Collot, "Synthetic aperture experiment in the visible with on-axis digital heterodyne holography," Opt. Lett. **26**, 1550–1552 (2001).

25. J. H. Massig, "Digital off-axis holography with a synthetic aperture," Opt. Lett. **27**, 2179–2181 (2002).

26. R. Binet, J. Colineau, and J-C. Lehureau, "Short-range synthetic aperture imaging at 633 nm by digital holography," Appl. Opt. **41**, 4775–4782 (2002).

27. Ch. Liu, Z. Liu, F. Bo, Y. Wang, and J. Zhu, "Super-resolution digital holographic imaging method," Appl. Phys. Lett. **81**, 3143–3145 (2002).

28. M. Paturzo, F. Merola, S. Grilli, S. De Nicola, A. Finizio, and P. Ferraro, "Super-resolution in digital holography by two-dimensional dynamic phase grating," Opt. Express **16**, 17107–17118 (2008).

29. L. Granero, V. Micó, Z. Zalevsky, and J. García, "Superresolution imaging method using phase-shifting digital lensless Fourier holography," Opt. Express **17**, 15008–15022 (2009).

30. V. Micó, L. Granero, Z. Zalevsky, and J. García, "Superresolved phase-shifting Gabor holography by CCD shift," J. Opt. A: Pure Appl. Opt. **11**, 125408 (2009).

31. W. Xu, M. H. Jericho, I. A. Meinertzhagen, and H. J. Kreuzer, "Digital in-line holography for biological applications," Proc. Natl. Acad. Sci. USA **98**, 11301–11305 (2001).

32. G. Pedrini and H. J. Tiziani, "Short-coherence digital microscopy by use of a lensless holographic imaging system," Appl. Opt. **41**, 4489–4496 (2002).

33. L. Repetto, E. Piano, and C. Pontiggia C, "Lensless digital holographic microscope with light-emitting diode illumination," Opt. Lett. **29**, 1132–1134 (2004).

34. J. Garcia-Sucerquia, W. Xu, S. K. Jericho, P. Klages, M. H. Jericho, and H. J. Kreuzer, "Digital in-line holographic microscopy," Appl. Opt. **45**, 836–850 (2006).

35. V. Micó, J. García, Z. Zalevsky, and B. Javidi, "Phase-shifting Gabor holography," Opt. Lett. **34**, 1492–1494 (2009).

36. U. Schnars and W. P. Jueptner, *Digital Holography* (Springer, 2005).

37. H. Jiang, J. Zhao, J. Di, and Ch. Qin, "Numerically correcting the joint misplacement of the sub-holograms in spatial synthetic aperture digital Fresnel holography," Opt. Express **17**, 18836–18842 (2009).

38. G. Pedrini, P. Fröning, J. H. Tiziani, and F. M. Santoyo, "Shape measurement of microscopic structures using digital holograms," Opt. Commun. **164**, 257–268 (1999).

39. S. De Nicola, P. Ferraro, A. Finizio, S. Grilli, and G. Pierattini, "Experimental demonstration of the longitudinal image shift in digital holography," Opt. Eng. **42**, 1625–1630 (2003).

40. http://www.schott.com/advanced_optics/english/download/datasheet_all_english.pdf.

41. P. Picart and J. Leval, "General theoretical formulation of image formation in digital Fresnel holography," J. Opt. Soc. Am. A **25**, 1744–1761 (2008).

42. D. P. Kelly, B. M. Hennelly, N. Pandey, T. J. Naughton, and W. T. Rhodes, "Resolution limits in practical digital holographic systems," Opt. Eng. **48**, 095801 (2009).